Generalized network modelling of two-phase flow in a water-wet and mixed-wet reservoir sandstone: Uncertainty and validation with experimental data

Ali Q. Raeini [*], Luke M. Giudici, Martin J. Blunt, Branko Bijeljic

Department of Earth Science and Engineering, Imperial College London, SW7 2AZ, UK

ABSTRACT

We use a generalized pore network model in combination with image-based experiments to understand the parameters that control upscaled flow properties. The study is focued on water-flooding through a reservoir sandstone under water-wet and mixed-wet conditions. A set of sensitivity studies is presented to quantify the role of wettability, pore geometry, initial and boundary conditions as well as a selection of model parameters used in the computation of fluid volumes, curvatures and flow and electrical conductivities.

We quantify the uncertainty in the model predictions, which match the measured relative permeability and capillary pressure within the uncertainty of the experiments. Our results show that contact angle, initial saturation, image quality and image processing algorithm are amongst the parameters which introduce the largest variance in the predictions of upscaled flow properties for both mixed-wet and water-wet conditions.

1. Introduction

Reliable prediction of upscaled flow properties of porous media is one of the main challenges in the energy sector, groundwater resource management and environmental science as well as in industrial applications that rely on flow through granular and fibrous media. Examples of the macroscopic properties – upscaled representation of molecular to pore-scale forces – are relative permeability (k_r) (Øren et al., 1998; Valvatne and Blunt, 2004), capillary pressure (P_c) (Moss et al., 1999), resistivity index (RI) (Archie, 1942; Glover, 2016), dispersion coefficient (Sahimi, 2011; Bijeljic et al., 2011) and reaction rates (White and Brantley, 2003; Al-Khulaifi et al., 2019). These properties, in particular P_c, k_r and RI, are functions of fluid saturation, displacement scenario, as well as fluid and solid properties such as wettability and pore geometry (Morrow, 1970; Armstrong et al., 2012). Furthermore, predictions of these properties may be subject to high natural, measurement or simulation uncertainty (DiCarlo et al., 2000; Reynolds and Krevor, 2015; Ramstad et al., 2020; Zahasky et al., 2020).

Traditionally the macroscopic flow properties of porous media have been estimated by matching empirical or numerical models to experimental measurements of pressures and average saturation (Oak, 1988; DiCarlo et al., 2000; Reynolds and Krevor, 2015; Moghadasi et al., 2016). A quantification of the uncertainty in these measurements, however, has rarely been presented. This poses a challenge for modelling studies: for a statistically valid comparison of predicted properties with experiment, the values should be similar to within the range of uncertainty in both the experiment and model itself. Without a proper evaluation of experimental uncertainty, this comparison is of a somewhat subjective nature, particularly when these uncertainties are large.

Several different methods have been developed over the past decades to predict the macroscopic properties of porous media, including pore network models (Øren et al., 1998; Valvatne and Blunt, 2004; Gostick et al., 2016; Regaieg and Moncorgé, 2017; Raeini et al., 2018) and numerical models that simulate flow directly on images of the pore-space (Tartakovsky and Meakin, 2006; Raeini et al., 2014; Pereira Nunes et al., 2016; Alpak et al., 2016; Akai et al., 2019a; Gago et al., 2021). Direct simulations are computationally expensive for many practical applications that require running sensitivity studies and uncertainty quantification on relatively large flow domains (Regaieg et al., 2021). Pore network models, on the other hand, require extensive validation to be considered reliable for the prediction of macroscopic flow properties. Recent advances in direct numerical simulations and experimental pore-scale measurements have provided the necessary data for their validation and refinement (Andrew et al., 2014a; Yang et al., 2017; Singh et al., 2017; Gao et al., 2020). Pore network models in turn are efficient tools for understanding and optimizing decision variables that influence the pore-scale physics of the industrial or environmental processes under consideration.

* Corresponding author.
E-mail address: a.q.raeini@gmail.com (A.Q. Raeini).

Nomenclature

ΔP	Pressure drop along the sample (Pa)
γ	Corner half angle angle
$\langle \Delta \rangle$	Mean signed difference
μ	Fluid viscosity
ϕ	Porosity
θ	Contact angle
A	Cross-sectional area
C	Coefficient
FF	Formation resistivity factor
g	Throat conductivity
I	Grey-scale intensity values in a micro-CT image
k_{abs}	Absolute permeability (Darcy)
k_r	Relative permeability
L	Length of core sample
P_c	Capillary pressure (Pa)
Q	Flow rate
R	Inscribed radius
RI	Electrical resistivity index
S	Saturation
BC	Boundary condition
Dif	Differential imaging
DNS	Direct numerical simulation
Exp	Experimental
GNM	Generalized network model
MW	Mixed-wet
SCAL	Special core analysis
seg	Segmentation
WW	Water-wet

Subscripts and superscripts

e and q	Electrical and volumetric flow
o	Oil phase
p	Pore
s	Solid phase
t	Throat
w	Water phase
wi	Initial water before water-flooding

Fig. 1. An illustration of different data sources for characterizing and minimizing uncertainty in the macroscopic description of multiphase flow through porous media. These include experimental image based special core analysis (SCAL), direct numerical simulation (DNS) and the generalized network model (GNM).

Their application of pore-space imaging allowed measurements of both capillary pressure and relative permeability from the same experiment. Another advantage of this type of data for validation of network models, compared to core-scale measurements, is the quantification of contact angles in situ at different stages of the displacement process.

In this paper we first quantify the uncertainty in the experimental data generated by Gao et al. (2020) and then use this data to validate the upscaled flow properties predicted using the generalized pore network model (GNM) (Raeini et al., 2018). Finally, the generated X-ray images of the pore space are used to build different digital realizations of the pore space using the GNM and to study the effect of various pore-scale parameters on the macroscopic two-phase flow properties.

This work complements our previous study on water-wet porous media (Raeini et al., 2019) where we quantified uncertainty in the average fluid occupancy to be typically less than 5% between pairs of repeated unsteady-state experiments by Andrew et al. (2014b), while the local pore-by-pore occupancy uncertainty was of the order of 5%–20%. The discrepancy between the GNM and experiments was less than 10% for the average saturation and occupancy and between 20%–30% in their local pore-by-pore counterparts. Note that these differences, even for repeat experiments on exactly the same sample, are sizeable. The implication is that the uncertainty in both the measurement and modelling of pore-scale processes need to be quantified carefully. This is the focus of this paper.

In the following section, we discuss the workflows used in this paper. Then, in Section 3, we present an evaluation of the uncertainty in the experimental data, which is principally due to ambiguities in image segmentation to find saturation and the measurement of pressure difference. Afterwards, in Section 4, we show a comparison between the GNM results and the experimental data while taking into account the effect of uncertainty in input contact angle and initial water saturation on network model predictions. In Section 5, the contribution of various input parameters describing the sample wettability, pore geometry and initial and boundary conditions, as well as the approximations used in the GNM are quantified through sensitivity studies. The results are used to draw conclusions on relative importance of these parameters for further refinement of experimental protocols and pore network models.

2. Methodology

This study aims to move towards integrating our experimental and modelling tools to better understand the mechanisms controlling two-phase flow through porous media and to reduce uncertainty in measuring or predicting them, as illustrated in Fig. 1.

Similarly, experimental techniques together with imaging of fluid phases in porous media have been used to investigate two-phase flow mechanisms in micro-model experiments (Keller et al., 1997; Chapman et al., 2013; Yang et al., 2017) and in X-ray imaging experiments on natural or synthetic porous media (Wildenschild and Sheppard, 2013; Andrew et al., 2014a; Fogden et al., 2015; Scanziani et al., 2017). The data generated experimentally have been used to investigate wettability characteristics of porous media (Andrew et al., 2014a; Alhammadi et al., 2017; Rucker et al., 2020) and displacement parameters such as the effect of flow rate (Zhang et al., 2021; Spurin et al., 2019). Furthermore, the results have been used to evaluate the accuracy of direct simulations (Akai et al., 2019a) as well as pore-network models (Bultreys et al., 2018; Raeini et al., 2019; Foroughi et al., 2021).

This work uses the experimental data by Gao et al. (2020) who simultaneously measured the pressure difference across a reservoir sandstone sample while imaging the rock and fluids within it. The experiments were steady-state injection of brine and oil into the same reservoir sandstone sample under two wettability conditions, before and after exposing the sample to a crude oil at high temperature.
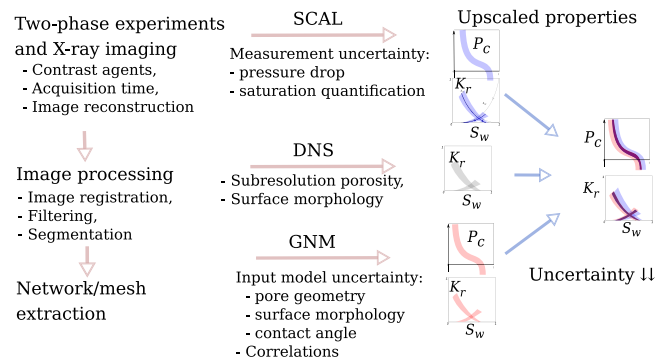
2.1. Image based special core analysis (SCAL)

The experimental data used in this paper are discussed in detail in Gao et al. (2020) who performed steady-state co-injection of oil and brine into a reservoir sandstone at several steps of increasing water fractional flows while recording the pressure difference between the injecting and receiving pumps. During each fractional flow experiment, micro-CT images of the whole sample, 32 mm in length and 6 mm in diameter were taken at a voxel size of 6.35 μm, as well as zoomed-in scans of the middle part at a voxel size of 3.58 μm. The experiments were repeated after exposing the sample to a crude oil at a high pressure and temperature to alter its wettability from water-wet to mixed-wet. Additionally, images of the sample in dry and fully brine saturated states were taken, by Gao et al. (2020), which are used in this study to obtain different representations of the pore space for network extraction. The zoomed-in images of the sample during oil–brine flow were further analysed by Gao et al. (2020) to obtain capillary pressure and contact angles. The contact angles were computed using an automatic algorithm (AlRatrout et al., 2017) and using energy balance (Blunt et al., 2019). In this work we have re-evaluated the uncertainty in the estimations of fluid saturations, relative permeability and capillary pressure which is discussed below.

The saturations used in this paper were computed by applying differential imaging to the experimental images. The differential imaging technique and the assessment of the uncertainty in the measured saturations are discussed in Appendix A. This involves first rescaling the grey-scale intensity values to have the same values for the voxels of the tubing (sample holder) and the impermeable parts of the solid matrix. Then individual images were subtracted from the brine saturated image and the intensity values of the brine and oil phases were sampled at different locations along the sample whose standard deviation is used to estimate the range of saturations as described in Appendix A.

The pressure difference was measured between the fluid injection and receiving pumps, which account for the pressure drop across the sample (ΔP), assumed to be the same in both phases, as well as the pressure drop in the tubing (Gao et al., 2020). These measurements have a low uncertainty themselves; the issue is the pressure difference in the tubing connecting the pumps to the sample during two-phase flow, which was comparable to the pressure drop across the rock itself and was estimated in separate experiments performed without the sample present. We assume that the pressure difference across the sample has an uncertainty of the same magnitude as the tubing pressure drop (see Appendix B) which are converted to uncertainty ranges in relative permeability using the multiphase Darcy law:

$$Q = \frac{k_{\mathrm{abs}} k_r}{A \mu} \frac{\Delta P}{L}, \tag{1}$$

where Q represents the flow rate of each phase and k_r is the phase relative permeability. Finally, k_{abs}, A and L are, respectively, single-phase permeability, cross-sectional area and length of the sample.

The capillary pressures (P_c) were computed by Gao et al. (2020) from the curvature of imaged fluid–fluid interfaces:

$$P_c = \sigma k_c, \tag{2}$$

where $k_c/2$ is the mean interface curvature and σ is the interfacial tension, 0.051 N/m in this study. However, the uncertainty range in the measured P_c is re-estimated in this work based on the analysis by Akai et al. (2019b). The average uncertainty in the water-wet case capillary pressure was estimated to be 820 Pa (30% of measured average capillary pressure) and is assumed to be the same for all fractional flows for both water-wet and mixed-wet experiments. A more accurate quantification of uncertainty and how to minimize it, however, is subject to future work.

The estimated uncertainties in the experimental Pc and k_r curves are presented in Section 3.

2.2. Direct simulations on images of fluid phases

We have presented an analysis of single-phase flow conductivities using direct numerical simulations (DNS) in Appendix E.1. These results show that both image resolution and segmentation algorithm can affect the quantification of single-phase flow properties. Additionally, in Appendix E.1, we show that introducing surface roughness is necessary for the direct simulations to match the measured porosity and permeability of the sample simultaneously.

It also is possible to estimate relative permeability using DNS on the images of individual fluid phases obtained during the two-phase flow experiments (Hussain et al., 2014; Berg et al., 2016). However, due to the high sensitivity of conductances to the inscribed radii of flow paths, this approach requires high resolution and sharp images of the fluid–fluid and fluid–solid boundaries. Therefore, we expect the errors associated with this approach to be higher compared to the conductivities obtained directly from pressure drop measurements, or from direct two-phase flow simulation that considers viscous coupling between the phases. Nevertheless this approach is presented in Appendix E.2 to provide an alternative estimation of upscaled properties which can be used to evaluate the effect of imaging artefacts and the segmentation of the images into different fluid and rock labels.

2.3. Generalized network modelling of two-phase flow

The third approach in Fig. 1 is to use the generalized network model, GNM, to predict capillary pressure and relative permeability. The GNM incorporates a rich representation of geometry extracted from the micro-CT images, while simulating pore-scale phenomena such as layer flow, contact angle hysteresis, snap-off and cooperative pore-body filling; see Raeini et al. (2017, 2018) for details of the GNM algorithm. Here, we mainly focus on studying its inputs and the main parameters that describe the approximations used in this model.

To extract a network of the pore space, images should be first segmented; the segmentation algorithm and thresholds can affect the properties of the extracted network and flow simulation results. To account for the effect of the segmentation, we run the network on: (i) the segmentation reported in the original work (Gao et al., 2020); (ii) a segmentation of the pore space using a multi-label clustering algorithm described in Appendix C; (iii) a representation of the pore space obtained using the clustering algorithm but with an altered surface morphology to account for sub-resolution surface features that can be missed after image reconstruction and segmentation (Schlüter et al., 2014) and finally (iv) an image (called Rock A, provided by TotalEnergies) of another sample drilled from the same sandstone core at a higher resolution of 1.5 μm.

The measured contact angles can be uncertain and affected by the image processing steps. Contact angles computed geometrically (AlRatrout et al., 2017) correspond to interfaces that are stable and hence may take any value between their advancing and receding values. Furthermore, despite the detailed images of fluid phases at several snapshots during the experiment, the time resolution of the micro-CT images is limited and we can only obtain average measures of the contact angle distribution. Therefore, here we do not adjust contact angles on a pore-by-pore basis but instead assign them statistically based on the analysis by Gao et al. (2020) using the thermodynamic approach (Blunt et al., 2019) as it measures the overall behaviour of the system during displacement.

In the generalized network model, GNM, we use geometrical approximations to compute interfacial curvatures and fluid saturations and correlations to compute fluid conductivities. These are further explained in Raeini et al. (2018), where the development of the model has been guided through analytical approximations and direct two-phase flow simulations on synthetic geometries. Furthermore, a description of the conductivity correlations are given in Appendix D. The aim of this study is to evaluate the reliability of the correlations used in the GNM

using micro-CT based experimental data, find potential areas for future improvement and, more importantly, to quantify the role of important parameters that control two-phase flow through porous media.

All GNM simulation results presented in this work correspond to water flooding cycle after primary drainage (oil injection). During primary oil injection the rock is assumed to be water-wet (receding contact angles of zero) but its end point (initial condition for the water-flooding cycle) is considered to be uncertain and is investigated through the sensitivity studies. As a base case, we run the primary drainage cycle up to a capillary pressure of 20 kPa.

2.4. Sensitivity studies on network model predictions

The uncertainty in the GNM predictions originate both from the uncertainty in the model inputs and from the approximations used in the model. The sensitivity to contact angle is performed by varying the mean value or spread (standard deviation) of the measured distribution. For other parameters which we have not quantified based on experimental data (such as wettability, spatial correlation length, corner connectivity and surface morphology) we simply choose a plausible range and compute the change in the upscaled properties compared to the base case values. The base case is a simulation where all parameters are kept as close as possible to experimental data, as discussed in Section 4; except for the parameter for which the sensitivity study is being performed, whose base value is set to the mid value between its lower and upper bounds (discussed in Section 5).

The uncertainties are presented in terms of mean signed deviation, $\langle \Delta \rangle$, and mean absolute deviation, $\langle |\Delta| \rangle$, from the base case values:

$$\langle \Delta \varphi \rangle = \frac{\sum (\varphi_{\text{upper}} - \varphi_{\text{lower}})}{2N} \quad (3)$$

$$\langle |\Delta \varphi| \rangle = \frac{\sum (|\varphi_{\text{upper}} - \varphi_{\text{base}}| + |\varphi_{\text{upper}} - \varphi_{\text{base}}|)}{2N} \quad (4)$$

where φ_{base} is the base case results of an upscaled property: capillary pressure P_c, porosity (ϕ), saturation S_w, absolute (k_{abs}) or relative (k_{rw} and k_{ro}) permeabilities, formation factor (FF) or resistivity index (RI). φ_{upper} and φ_{lower} are the upscaled property values corresponding to the upper and lower bounds of the parameter for which the sensitivity analysis is being performed (e.g. contact angle, initial water saturation; see Section 5). Finally, the summations ($\sum$) are performed over N which is equal to the number of times the sensitivity analysis is repeated multiplied by the number of data points describing each property. All sensitivity studies presented in this paper are repeated for the four different representations of the void space discussed in the previous section. Therefore, $N = 4$ for single-phase properties ($\varphi = \phi$, k_{abs} or FF) which are described using one data point per simulation. For saturation dependent data ($\varphi = P_c$, k_{rw}, k_{ro} or RI) $N = 40$ since we sample them at ten equally distanced saturation intervals for each simulation. The differences are computed in linear space, for the sake of simplicity, which implies that larger relative permeability values contribute more to the reported differences. Nevertheless, this analysis leads to a quantification of the relative importance of the input or model parameters for predicting the upscaled flow properties which are presented as bar charts in Section 5.

3. Experimental results

Fig. 2 presents the experimental results by Gao et al. (2020) with our evaluation of fluid saturations and uncertainty in capillary pressure and relative permeability as discussed in Section 2.1.

The fluid saturations presented in Fig. 2 are obtained using differential imaging (see Appendix A). In this experiment a 3.5% solution of Potassium Iodide was used to improve the water (brine) phase X-ray attenuation and increase its contrast with the oil. The uncertainty in the differential imaging analysis can be reduced by increasing the contrast

between the brine and oil phase; however this needs to be optimized to firstly ensure a linear relationship between the phase contrast and fluid saturation and secondly to avoid image blur due to excessive blockage of the X-ray signal by the contrast agent.

The uncertainty in relative permeability can also be further reduced by a more accurate quantification of the pressure difference across the sample and the tubing, which can be substantial when using viscous fluids in the experiment. Nevertheless, a similar level of uncertainty can be deduced from experimental data obtained using traditional core-scale experiments (DiCarlo et al., 2000; Reynolds and Krevor, 2015), potentially due to the impact of core-scale heterogeneity on flow at low capillary numbers.

The effect of various descriptors of the model and its inputs on the predicted macroscopic two-phase flow properties are investigated using the GNM in the following sections.

4. Generalized network flow simulations

In this section, we demonstrate the sensitivity of the GNM predictions on contact angle, on initial capillary pressure at the beginning of water-flooding and on the image segmentation algorithm, which were three of the most important input parameters of the GNM model. The GNM results are compared with their experimental counterparts in Fig. 3. As described previously, the range of contact angles used in the GNM simulations are chosen based on the experimentally measured values using the energy balance approach: 20–80° for the water-wet (WW) case and 40–120° for the mixed-wet (MW) case (Gao et al., 2020, Fig. 8C). The contact angles assigned to pores are chosen from this range assuming a normal distribution with a standard deviation equal to 25% of the contact angle range ($50 \pm 15°$ for the WW and $80 \pm 15°$ for the MW case), and using a spatial correlation length of 2 ± 1 pores (AlRatrout et al., 2018). The spatial correlation is achieved by clustering adjacent pores into groups of 2 ± 1 pores and assigning a single contact angle to all pores in a cluster. The range of uncertainty in the upscaled flow properties in Fig. 3 are obtained by shifting the mean of the contact angle distribution by $\pm 20°$.

The simulations are presented on the four segmentations of the pore space discussed in the previous section. The sandstone used in this study is considered a clean sandstone—predominantly made of quartz grains. Our segmentation of the clay phase from the micro-CT images indicated that only 0.3% of the bulk volume is made of clay minerals. Therefore, in the simulations we assume that clay accounts for 1.5% of the pore volume (0.3% of total volume) which contains immobile water. This, however, is considered uncertain and hence is included in the uncertainty studies presented in Section 5.

The initial condition for the water-flooding simulation is obtained by running a primary drainage simulation down to a specific water saturation or capillary pressure. The initial capillary pressure of the experiment cannot be quantified from curvature measurements due to the limited resolution of the X-ray images. The initial water saturation is estimated using differential imaging to be $12 \pm 8\%$. Similarly, in this work we run the drainage simulation down to water-saturations of $12 \pm 8\%$ to investigate the effect of initial condition on the predicted capillary pressure and relative permeability.

The GNM and experimental results overlap, albeit with considerable uncertainty ranges. The differences between the experiment and model in many cases can be attributed to the finite resolution of the 3D images of the pore space and the network model, the differences in the wettability of the simulations and the experiment, and also to the differences in the treatment of boundary and initial condition at the beginning of water-flooding. In the following section we present a more detailed quantification of the uncertainties introduced due to different descriptors of wettability, pore geometry, initial and boundary conditions as well as an assessment of a selection of the model parameters used in the correlations and approximations of capillary entry pressures, fluid volumes and conductivities. These sensitivity studies
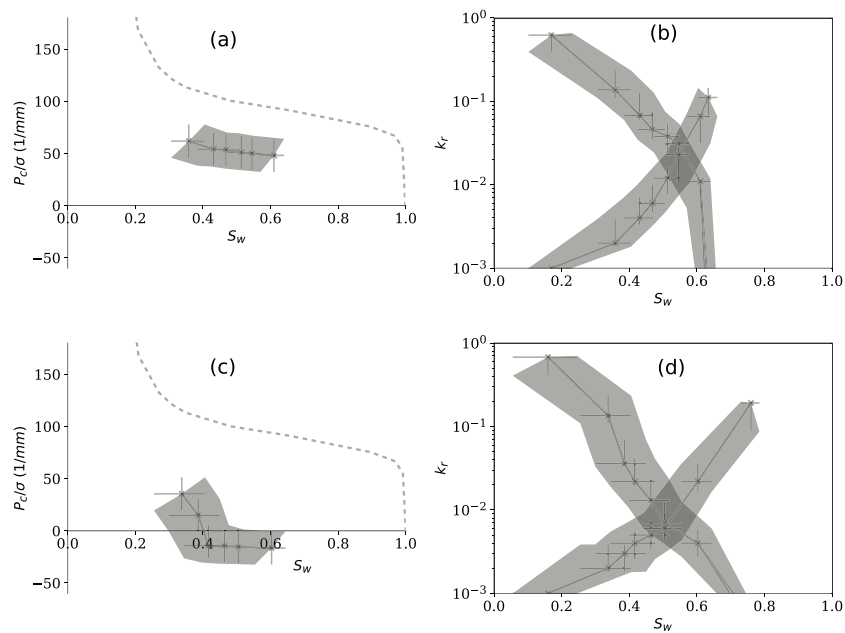
Fig. 2. Water-wet (a,b) and mixed-wet (c,d) experimental capillary pressure (a,c), and relative permeability (b,d) (Gao et al., 2020) versus saturation and their re-evaluated uncertainty ranges (shaded areas). The dashed line in (a,c) corresponds to a mercury-injection capillary pressure measurements for primary drainage while the remaining plots correspond to the steady-state water-flooding experiments. The initial point in P_c is eliminated because the image resolution is insufficient for accurate curvature computation. The initial saturation and relative permeability can be read from the left-most points of the relative permeability plots; see also Table B.1.
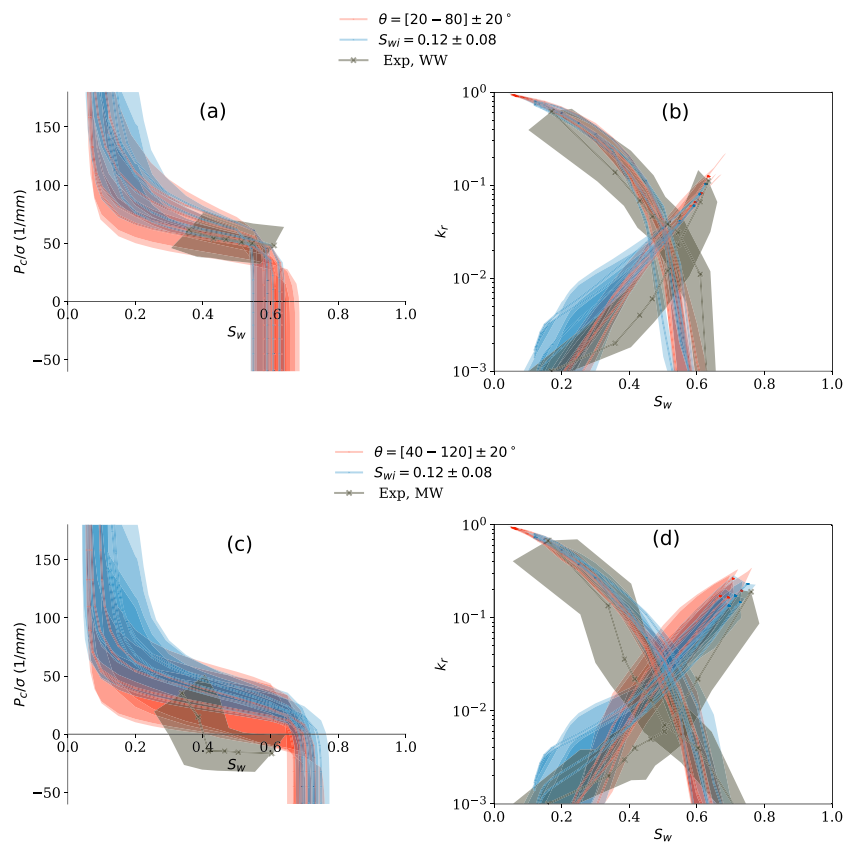
Fig. 3. A comparison between GNM predictions of capillary pressure, P_c, and relative permeability, k_r with micro-CT based experimental data. The GNM simulations presented show the sensitivity study on mean contact angle and on initial water saturation at the beginning of the water-flooding cycle, for the four different representations of the void space. As shown in the figure legends, the initial water saturation is varied in the range of $12 \pm 8\%$ and the contact angle is varied by $\pm 20°$.

together with further comparisons with more experimental data and with high resolution direct two-phase flow simulations on benchmark

geometries are necessary to quantify these discrepancies and further improve our pore-scale experimental and modelling workflows.

5. Uncertainties in GNM predictions

In this section, to have a more comprehensive but compact quantification of the sensitivity, we average the uncertainty ranges of each upscaled property (S_w, k_{rw}, k_{ro}, RI, k_{abs}, FF) to obtain a single value for the impact of various input or model parameters on the upscaled flow property. The results of sensitivity studies are further averaged over the simulations that have been performed over the four representations of the void space discussed in Section 2.3 and are presented as bar charts. The input and model parameters are divided into (i) descriptors of wettability distribution, (ii) pore geometry, (iii) initial and boundary conditions and (iv) model approximations.

5.1. Wettability

Fig. 4 shows the effect of uncertainty in the input parameters describing the wettability of the sample:

Advancing contact angle: The effect of advancing contact angle is analysed by shifting the mean of the contact angle distribution by $\pm 20°$ compared to the base case values discussed in the previous section.

Advancing contact angle range: The effect of the range of contact angle is analysed by shrinking and expanding the contact angle range (twice the standard deviations) by $\pm 10°$ while keeping its mean value same as the base case.

Contact angle radius correlation: In this sensitivity study, the radius correlation for contact angles is changed from uncorrelated to rank correlation coefficients of ± 1 with the inscribed radius.

Wettability spatial correlation: The wettability spatial correlation of contact angle is varied by a factor of two, from a lower range of 1–2 pores to a mid case of 2–4 pores and a higher range of 4–8 pores. The spatial correlation is implemented by clustering adjacent pores to randomly selected seed pores until all pores are selected. The spatial correlation length represents the number of pores in the clusters. The contact angle assigned to each cluster is chosen from a normal distribution with mean and standard deviations of $50 \pm 15°$ for the water-wet, WW, simulations and $80 \pm 15°$ for the mixed-wet, MW, case—same as the base case.

The results in Fig. 4 indicate that the contact angle values and their distribution over the network play an important role in determining the upscaled flow properties, hence indicating further research in this field is needed to better quantify them for various porous media types and fluids. While we can assign a reliable average contact angle from energy balance, we cannot, at present, determine precisely pore-by-pore values.

5.2. Pore space geometry

Fig. 5 shows the effect of uncertainty in the input parameters describing the pore space geometry, which are described below.

Corner connectivity number: Corner elements in our model are assumed to be connected to 0, 1 or 2 other corners from each side. This is assigned based on proximity of corners and is not currently extracted directly from the underlying image. We only allow two corners to be connected if their medial axes make an angle less than $90°$. To study the impact of this parameter, here we further restrict the connectivity of some of the corners at random to account for potentially lower connectivity in the underlying image, with probabilities of 0 (base case), 16.6% and 33%. This means that the probability that a corner is connected to another corner from each side will be reduced from 1 to 0.834 and 0.67, respectively.

Sub-resolution water: Sub-resolution water accounts for water absorbed in clay minerals or residing in small pores and crevices not resolved in the micro-CT image. These pores are assumed to have high capillary entry pressures and therefore remain water-filled during the experiment and do not have a major contribution to flow conductivity due to their small size. However, they do contribute to water saturation
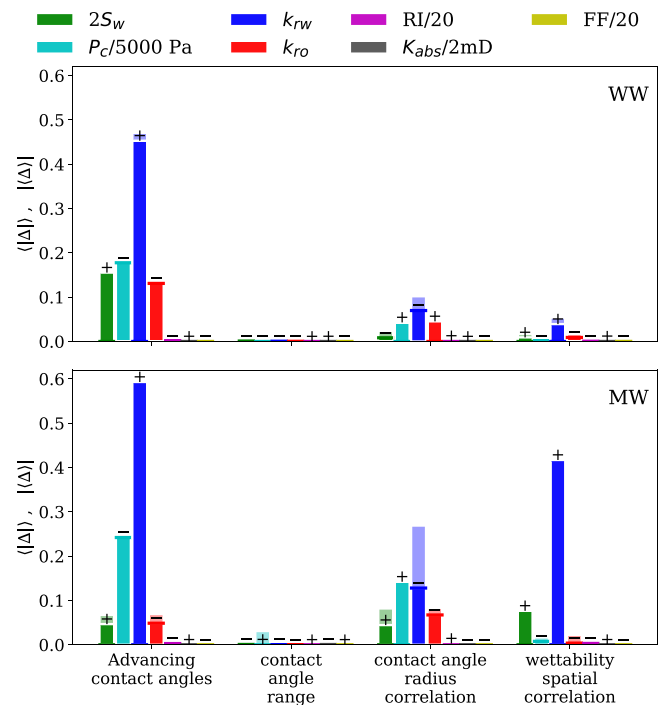

Fig. 4. Effect of uncertainty in the descriptors of contact angle distribution – mean value, spread, correlation with inscribed radius and spatial correlation length – on the upscaled properties. The lighter (and taller) bars show the mean absolute deviation, $\langle |\Delta \varphi| \rangle$ where φ is the parameter indicated in the plots' legend. The darker bars show the magnitude of the mean signed deviations, $|\langle \Delta \rangle|$, whose signs are indicated by the + or − symbols on top of them. Note that when the rank correlation coefficient between an upscaled property and a sensitivity parameter is ± 1, the bars showing the two measures of sensitivity fully overlap and only the dark colour is visible. The uncertainty ranges of the macroscopic properties are normalized based on an average value, as indicated in the plot legends, to make them presentable in the same graph.

and electrical conductivity. The results in Fig. 5 are obtained from simulations where volume fractions of 0, 1.5% (base case) and 3% of void space (0, 0.3 and 0.6% of total volume, respectively) are assigned to these sub-resolution pores. The sandstone used in this study is a clean sandstone—containing a small clay fraction compared to many sandstones found in hydrocarbon reservoirs. Therefore the sensitivity study presented here can underestimate the uncertainty in such cases.

Voxel size: The effect of voxel size is studied using the image of the Rock-A sandstone, which was drilled from the same rock formation used in the rest of our analysis but was scanned at a smaller voxel size of 1.5 μm by TotalEnergies. It is then coarsened by factors of 1, 2 and 3 to study the effect of voxel size, 1.5, 3 and 4.5 μm, respectively. Note that this analysis does not account for imaging artefacts when scanning the image at coarser resolutions where other factors such as image blur and signal-to-noise ratio can play a role too; it solely accounts for the role of the image resolution used in the network extraction and its impact on flow simulations.

Surface morphology: Micro-CT images often have a degree of image artefacts such as a blur between the grey-scale values of the pore-space fluids and the minerals. Consequently, their segmentation can lead to images of the pore surfaces that are smoother than the actual geometry. To study the effect of surface morphologies that can be removed during the image processing, we alter the voxels on either side of grain walls with a probability of 25% iteratively, for 0, 2 and 4 iterations. These images are then used in the network extraction and flow model to predict the impact of surface morphologies at the scale of the voxel size on the network model predictions.

The results in Fig. 5 show that voxel size and surface morphology play an important role in the accuracy of single-phase flow simulation
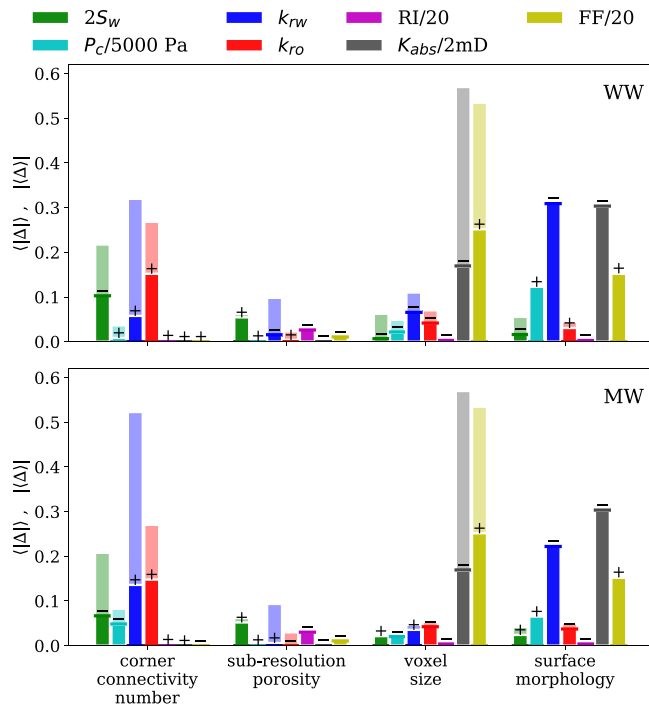
Fig. 5. Sensitivity of the upscaled properties to uncertainties in different descriptors of the pore space geometry, including mean corner connectivity number/probability, sub-resolution pores and crevices, voxel size and number of surface morphology alteration iterations. See the caption of Fig. 4 for the interpretation of the bar charts.

of formation factor and absolute permeability. Additionally, voxel size and corner connectivity number have a significant impact on two-phase flow properties.

5.3. Initial and boundary conditions

Fig. 6 shows the results of our sensitivity analysis on the input parameters that describe the initial condition at the beginning of the water-flooding simulation and the boundary conditions that control the flow rates and contribution of viscous pressure in the displacement process:

Viscous pressure drop: In this analysis, both phase viscous pressure drops were equal and set to $\Delta P_w = \Delta P_o = 32, 320$ and 3200 Pa ($6.2, 62$ and 620 kPa/m) which partially covers the range of pressure gradients recorded in the experiment (62–1680 kPa/m).

Water viscous pressure drop: Here the oil-phase pressure drop is kept at 1 Pa while the water phase viscous pressure drop is varied from $\Delta P_w = 1$ to 500 and 1000 Pa. Therefore, the simulation results represent the effect of capillary pressure gradient (for example due to boundary effects) which can lead to a different pressure gradient in the two fluid phases.

Oil viscous pressure drop: Similar to the case of water-phase pressure drop, here the oil (non-wetting) phase viscous pressure drop is set to $\Delta P_o = 1, 500$ and 1000 Pa while the water-phase viscous pressure drop is kept at 1 Pa.

Upscaling bounds: The boundaries of the domain for which the flow properties are computed were set to 20%–90%, 25%–75% and 5%–95% of the length of the images which are cylindrical domains of length 1400 and diameter 1600 voxels in this paper. Note this parameter relates to heterogeneity of the displacement process and can behave differently depending on the physical scale of the flow domain and the relative importance of viscous forces.

Initial saturation: The capillary pressure at the end of drainage (initial condition for water-flooding) determines how much water is left in corners of the pore space or in small pores and throats. These water-filled elements in turn affect the capillary entry pressure computations and lead to a more water-wet behaviour compared to the case where water is drained down to a high capillary pressure. As stated in Section 4, we run the drainage simulation down to water-saturations of $12 \pm 8\%$ to investigate the effect of initial condition on the computed flow properties using the GNM.

The results in Fig. 6 show that initial saturation/capillary pressure plays a major role in controlling the displacement behaviour during water-flooding. The initial occupancy of brine has an impact on the whole displacement sequence: it is necessary to reproduce the starting state of the water-flood as accurately as possible (Bultreys et al., 2020). The viscous pressure drop and the size of the network used in the computation of upscaling properties have a smaller impact. This is to be expected, as the experiments were run in the capillary-controlled regime where viscous effects are small, and the network itself is sufficiently large to encompass a representative elementary volume (Mostaghimi et al., 2012).

5.4. Model parameters

In Fig. 7 we investigate the effect of a set of the GNM parameters that were found to have the largest impact on the prediction of upscaled flow properties. These parameters are not input parameters and hence the objective is not to quantify uncertainties but to better understand the model and find where further refinement of the model can be the most effective in improving its predictive power.

Piston-like curvature contribution to S_w: This coefficient is used as a first order correction for computation of fluid saturations in piston-like configurations. The volume of the phase toward the pore-centre (non-wetting phase) is set to that computed using linear interpolation of corner-level volumes (Raeini et al., 2018) minus this factor times the contact angle normalized by π. This factor is set to 1 ± 0.5 in the analysis presented here. This feature has not been implemented in our previous work, see Raeini et al. (2018, Eqn. (22)).

Pore sagittal curvature coefficient: Similarly, we modify the equation used for calculation of layer sagittal curvatures at pore centres, (Raeini et al., 2018, Eq (13)) by multiplying it with a constant factor of 0, 1 (base case) and 1.33. Corner sagittal curvatures in this analysis represent the interfacial curvature along the corner medial axis which is subtracted from the total curvature to obtain the curvature in axial cross-sections of the corners and in turn to obtain the snap-off threshold pressures and the volume-fraction of the water phase in the layers; see Raeini et al. (2018) for more details.

Conductance coefficient C_1: This coefficient is introduced to further investigate and calibrate the correlations used to compute flow conductivities of the corner levels, Eq. (D.3) in Appendix D. Here we chose $C_1 = 0.1 \pm 0.05$.

Piston-like conductivity coefficient: This is a correction factor multiplied by the interpolated conductivity of fluids under a piston-like configuration. Its values are chosen as 0.55 ± 0.45 in this analysis.

Fig. 7 shows that the conductance coefficient has a major effect on the single-phase permeability and formation factor, but has a smaller impact on the relative permeability. Another important observation is that the parameters used to approximate the volume of fluids in piston-like configurations have a relatively high impact on the saturation computations. In comparison, the sagittal curvature has a moderate impact on the upscaled flow properties. Although the impact of these parameters is lower compared to the impact of uncertainties in the inputs, in particular contact angle distributions, it is important to further calibrate the model using direct simulations so that it can be used as a complementary tool to better understand the experimental results and to perform more accurate case studies to optimize the microscopic performance of the two-phase flow processes of interest.

Overall this section has shown that the wettability, voxel size (image resolution) and initial conditions are the three most sensitive inputs
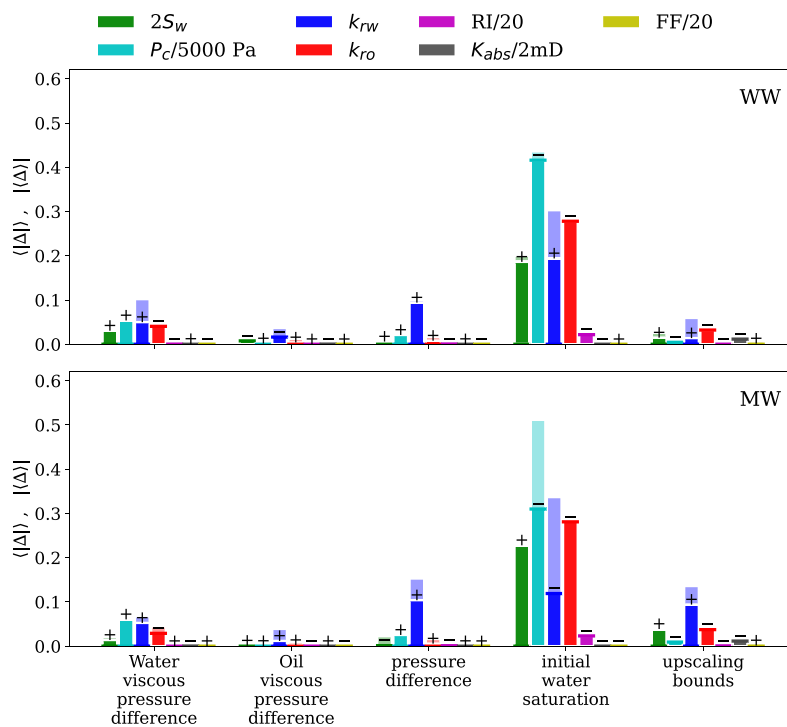
Fig. 6. Sensitivity of the upscaled flow properties to viscous pressure difference between inlet and outlet boundaries of the network for water, oil and both phases, to initial capillary pressure and to sample length used in the upscaling of saturation and flow conductivities. See the caption of Fig. 4 for the interpretation of the bar charts.
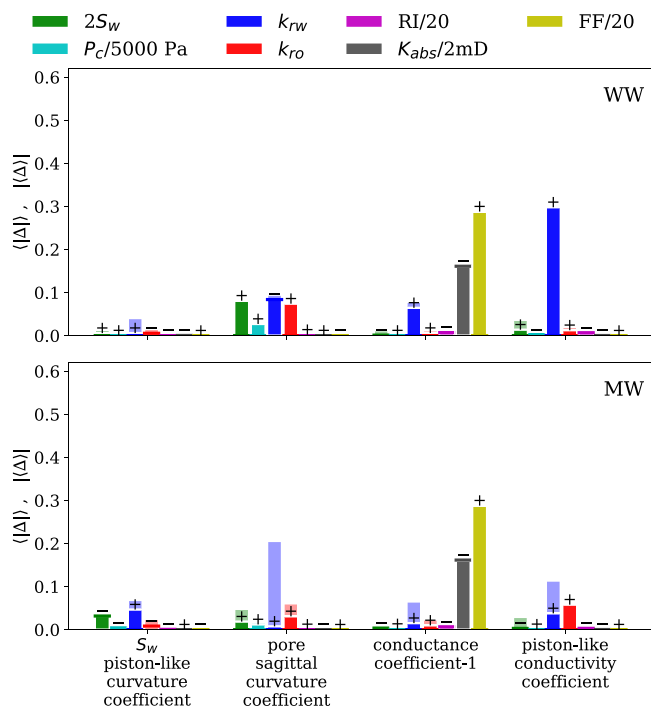

Fig. 7. Effect of a selection of model parameters used in computation of fluid saturations, curvatures and fluid conductivities on the upscaled flow properties. These parameters include the coefficients used in computation of piston-like curvature contribution to S_w, sagittal curvature in pores, conductivity correlations in single-phase and piston-like configurations. See the caption of Fig. 4 for the interpretation of the bar charts.

to pore-scale models. Even though high-resolution imaging can resolve most of the pore space, detailed features, such as pore wall roughness cannot be captured. Furthermore, while energy balance does provide a good average estimate of contact angle, it cannot yet be applied with sufficient precision to assign pore-by-pore values. The result is that there is a significant range of uncertainty in model predictions, which is mirrored by uncertainties in the experiments themselves, again related to image quality and the measurement of pressure differential. Future improvements in experimental protocols and imaging facilities should be able to reduce these uncertainties, and to increase the predictive power and applicability of this imaging and modelling workflow to a wider range of samples.

6. Conclusions

In this paper we have presented an overview of the uncertainty in micro-CT based experimental data and compared the results with network model predictions, considering the range of uncertainties in network model parameters that are used to compute fluid volumes and threshold curvatures as well as flow and electrical conductivities. Our results demonstrate that the generalized network model predictions are close to the range of the experimental data and hence the model can be used to study and optimize two-phase flow processes at the pore scale. Nevertheless, the complexities of two-phase flow through porous media introduces significant uncertainties in our experimental data and in the description of our pore-scale model inputs, which implies that a more integrated experimental and modelling approach is needed.

We have presented several sensitivity studies that show the potential of pore-scale models and reveal the pore-scale parameters that play an important role in displacement processes. These sensitivity analyses indicate that parameters such as wettability, pore geometry and surface morphology have a large impact on the upscaled flow properties. Minimizing the uncertainties these parameters introduce in our workflow, however, requires collecting more high quality experimental data with lower uncertainty ranges, as well as performing high-fidelity direct simulations to further improve our understanding of two-phase flow. Such data can be used to improve the network model predictions both in terms of local pore-by-pore parameters as well as upscaled flow properties.

CRediT authorship contribution statement

Ali Q. Raeini: Software, Investigation, Writing – original draft. **Luke M. Giudici:** Software, Writing – review & editing. **Martin J. Blunt:** Conceptualization, Supervision, Writing – review & editing. **Branko Bijeljic:** Conceptualization, Supervision, Writing - review & editing.

Declaration of competing interest

The authors declare that they have no known competing financial interests or personal relationships that could have appeared to influence the work reported in this paper.

Acknowledgements

Appendix A. Saturation uncertainty

Uncertainty in porosity and saturation can be estimated based on variations on grey-scale intensity (I) of different phases, assuming that they scale linearly with the volume fraction of each phase. The porosity can be estimated based on the intensity of the phases in the images:

$$\bar{I} = I_s(1 - \phi) + \phi I_a \tag{A.1}$$

$$\rightarrow \quad \phi = (\bar{I} - I_s)/(I_a - I_s) \tag{A.2}$$

where subscripts a and s stand for air and solid phase respectively and $\bar{I}$ stands for the average intensity of the whole image.

Similarly, fluid saturations can be estimated based on the intensity of the phases in partially-saturated images – containing oil (o), brine (b) and solid (s):

$$\bar{I} = I_s(1 - \phi) + I_o \phi S_o + I_w \phi(1 - S_o) \tag{A.3}$$

$$\rightarrow \quad S_o = \frac{\bar{I} - I_w \phi - (1 - \phi)I_s}{\phi(I_o - I_w)} \tag{A.4}$$

here $\bar{I}$ is the average intensity of the partially saturated image.

Differential imaging can be used to both simplify the equations and reduce the uncertainty in the measured porosity and saturations. When subtracting brine saturated image from the dry image, the solid phase intensities cancel out ($I_s \rightarrow 0$) and air and brine intensities are subtracted from each other (I_{a-w}). Therefore, Eq. (A.1) can be written as:

$$\phi = \frac{\bar{I}}{I_{a-w}} \tag{A.5}$$

Similarly, when subtracting the partially saturated image from the brine saturated image, brine and solid phase intensities cancel out and calling the subtracted oil and brine phase Intensity I_{o-w}, Eq. (A.3) yields:

$$S_o = \frac{\bar{I}}{\phi I_{o-w}} \tag{A.6}$$

Therefore, in differential imaging, the remaining sources of uncertainty are the intensity values for the void space in the differential image, I_{a-w}, and the differential value of the oil-invaded regions, I_{o-w}.

Additionally, increasing the contrast between the water and oil X-ray attenuations will lead to lower uncertainties. However, there is a trade-off as making one phase too opaque to X-ray leads to lower image quality and increased image blur which makes image segmentation less accurate.

Table B.1
Fluid saturations obtained using differential imaging, Eq. (A.6), and total pressure difference between injecting and receiving pumps and the tubing pressure drop, measured after each fractional flow experiment with the core sample removed (Gao et al., 2020).

Water-wet			Mixed-wet		
S_w (%)	Total ΔP (kPa)	Tubing ΔP (kPa)	S_w (%)	Total ΔP (kPa)	Tubing ΔP (kPa)
16.7 ± 6.4	4.34	2.18	15.4 ± 9.6	4.11	2.12
35.6 ± 5.0	11.42	2.16	33.3 ± 7.5	11.49	1.89
42.9 ± 4.4	18.77	2.18	37.8 ± 7.5	34.29	2.18
46.6 ± 4.1	26.42	6.13	41.2 ± 6.6	48.40	6.11
51.2 ± 3.8	26.72	9.30	46.0 ± 6.1	61.49	10.28
54.4 ± 3.5	26.70	13.10	50.1 ± 5.6	66.99	13.11
60.7 ± 3.5	12.09	5.68	60.0 ± 4.5	23.69	5.68
63.3 ± 2.8	6.16	2.36	75.8 ± 2.7	4.55	2.36

Appendix B. Experimental saturation and pressure difference

Table B.1 shows the re-evaluation of the uncertainty in the water saturations measured based on differential imaging discussed in Appendix A and in the measured pressure difference along the sample, which is assumed to be the same as the measured pressure drop in the tubing connecting the sample holder to the injecting and receiving pumps described by Gao et al. (2020).

Appendix C. Image segmentation

Our current flow simulation model uses, for simplicity, a segmented image for the description of the geometry. Typical micro-CT images have a blur of few voxels across the boundary between fluid and solid phases, and where the exact boundary is chosen during the image segmentation can affect the hydraulic radii of pore throats and fluid images. This in turn can have a major impact on the computed flow transmissibility which scales with the radius to the fourth power.

Although there has been previous research on different image segmentation approaches (Schlüter et al., 2014) for analysing micro-CT images of porous media, our understanding of the effect of image processing steps and the segmentation algorithm on the predicted single and multiphase flow properties is incomplete. Global thresholding algorithms such as the OTSU algorithm rely only on the grey-scale intensity histograms and do not perform well for 3D geometries and for multi-label segmentation. Other commonly used segmentation algorithms are watershed and WEKA machine learning, which has been investigated in Garfi et al. (2020) for their impact on image statistics and single-phase flow properties. Supervised WEKA machine learning incorporates the spatial distribution of the grey-scale intensities into account for selection of its local thresholds. However, it requires human input to set its internal parameters and its performance cannot be quantified separate from those inputs. Watershed segmentation uses the image intensity gradient to choose its thresholds to separate different regions of the image. In particular, it can avoid the segmentation of image blur (ring effects) into fluid layers. However, it cannot be used without extensive filtering if the image does not have relatively sharp boundaries between different regions or does not have high signal to noise ratio. Moreover, the location of maximum gradient may not necessarily be the optimal value for separating different image regions with varying sizes.

The algorithm presented in this section combines local and global thresholding approaches to have a relatively simple but flexible algorithm that aims to avoid the misclassification of image blur as an intermediate phase and yet allows small fluid layers to be identified. This however requires further investigation using a data driven approach to choose the parameters of the algorithm and of the image enhancement algorithm, such as the number of iterations and kernel sizes. In this work these parameters are simply chosen by visually

inspecting the resulting segmentation of the image and comparing it with the grey-scale image.

We first filter the images using a bilateral-mean with simultaneous bounded sharpening algorithm, where each voxel value is recursively altered based on weighted averages of its adjacent voxels as follows:

$$\delta v_{bl} = \frac{\sum w_b \delta v_j}{\sum w_b}, \qquad w_b = \frac{1}{1 + \delta v_j^2/\sigma_v^2 + dx_{ij}^2/\sigma_l^2} \tag{C.1}$$

$$\delta v_{sh} = \frac{\sum w_s \delta v_j}{\sum w_s}, \qquad w_s = \frac{\min(\delta v_j^2, \sigma_v^2)}{\epsilon + dx_{ij}^2/\sigma_l^2} \tag{C.2}$$

$$\delta v_{\min} = \frac{\sum w_m \delta v_j}{\sum w_m}, \qquad w_m = \text{step}(\delta v_j \le 0) \tag{C.3}$$

$$\delta v_{\max} = \frac{\sum w_x \delta v_j}{\sum w_x}, \qquad w_x = \text{step}(\delta v_j \ge 0) \tag{C.4}$$

$$v_i^{filt} = v_i + \min(\max(\delta v_{\min}, \ \delta v_{bl}(1 + f_{sh}) - f_{sh} \delta v_{sh}), \delta v_{\max}) \tag{C.5}$$

where δv_{bl}, δv_{sh}, $\delta v_{\min}$ and $\delta v_{\max}$ are changes to voxel values (v_i) using weighted bilateral, unsharp, max and min algorithms, which differ only in the choices of the weighting factors, w, as shown in the equations above. δv_j represents the difference between an adjacent (j) voxel intensity and the intensity of the voxel itself, v_i.

To segment the image, we first select an initial guess for different threshold values that separate the image into different labels by visually inspecting the grey-scale slices and their histograms. This initial guess is used to assign the seeds for a clustering algorithm. A voxel is chosen as a seed if it falls within 25–75 percentile of the threshold values for each region. Voxels that have adjacent voxels assigned to one or more of the segmentation regions are assigned to the region, g, with the lowest rank, $f_{i,g}$, which is computed for each voxel, v_i, and region pair:

$$f_{i,g} = \frac{|v_i - \overline{v_j^g}| \ (1 - f_G) + f_G \ |v_i - \text{med}(v^g)| + c_\sigma}{\min(1 + c_{sm} f_g, \ f_{cap})} \tag{C.6}$$

where med stands for median value of all voxels in the region; f_G is a weighting factor which, when set to a value closer to one, moves the algorithm toward a global thresholding algorithm; $\overline{v_j^g}$ is the average of adjacent voxels belonging to region g and $f_g = \sum w_j^g / \sum w_j$ is a measure of the fraction of the adjacent voxels belonging to region g. Having a larger value for f_g implies that small-scale features, whose segmentation purely based on the grey-scale values has a high uncertainty, are assigned to the label of the adjacent voxels with the highest frequency.

The image filtering and segmentation algorithms discussed above, and the image blur artefacts, effectively lead to a smoother representation of the solid surfaces compared to the actual pore geometry. This can be compensated by reintroducing roughness to the pore wall surface, by iteratively changing the voxels on either side of the void–solid boundary with a given probability. The resulting image with altered surface morphology is used as the fourth representation of the void space in our network extraction and flow modelling in this work.

Fig. C.8 shows a slice at the middle of the segmentation of the dry image by Gao et al. (2020) and the differential image (difference between dry and the fully brine saturated images) using the algorithm presented above. A screenshot showing the qualitative difference of the two segmentations is also presented, which highlight potential sources of uncertainty in direct simulation and pore network modelling results.

Both segmentations presented in Fig. C.8 under-predict the porosity while over-predicting the permeability, compared to the experimentally measured value; see Table E.3. This problem can be addressed by altering the surface morphology as shown in Table E.4. Further research is needed to have a reliable workflow for predicting these properties for different levels of imaging artefacts and different rock types.

Appendix D. Corner conductivity correlations

In the generalized network model, the pore space is divided into corner elements and each corner is further discretized into three sub-elements whose conductivities are, in this work, obtained using the correlations presented below. The corner level 1 represents single-phase flow. Corner levels 2 and 3 represent scenarios where voxels inside inscribed spheres larger than, respectively, 1 and 0.7 times the throat radius are filled with a different fluid than those deeper in the corner edge. Further details on how these correlations are used in the generalized network model are discussed in Raeini et al. (2018).

The corner electrical and flow conductivities (g_i^e and g_i^q, respectively), at discretization levels $i = 2$ and 3, are obtained using the following equations:

$$g_i^e = \tau_c \frac{A_i}{L_i}, \quad i = 2, 3 \tag{D.1}$$

$$g_i^q = \tau_c^2 (0.168 - 0.036\gamma_i) R_i^2 g_i^e, \quad i = 2, 3 \tag{D.2}$$

where R_i is the inscribed radius corresponding to the corner discretization level, A_i is its cross-sectional area, L_i is its length and τ_c is a tortuosity factor, set to 0.95 in this study.

To estimate the conductivity of corner centres, we first estimate them using the corner parameters at the throat surface:

$$g_1^{*e} = \frac{A_1 - C_1^g A_2}{L_1}, \tag{D.3}$$

$$g_1^{*q} = \frac{R_2^2 g_1^{*e}}{8 - 4A_2/A_1}, \tag{D.4}$$

where C_1^g is a coefficient used to perform sensitivity study and calibrate the conductivity correlations in Fig. 7.

The conductivities above are corrected for the effect of expansion of the half-throat cross-sectional area between the throat surface and the adjacent pore centres:

$$g_1^{**e} = g_1^{*e} R_{p/t} \tag{D.5}$$

$$g_1^{**q} = g_1^{*q} R_{p/t}^3 / (1 + \delta R_{p/t} + \delta R_{p/t}^2 / 3) \tag{D.6}$$

where $R_{p/t} = \frac{R_p}{R_t}$ and $\delta R_{p/t} = \frac{R_p - R_t}{R_t}$ are the expansion ratio and the relative expansion of the maximal-sphere radius from the throat centre to the pore centre.

Finally, the corner conductivities at level $i = 2$ are added to these conductivities to obtain the level 1 (single-phase flow) conductivities.

$$g_1^e = g_1^{**e} + g_2^e, \tag{D.7}$$

$$g_1^q = g_1^{**q} + g_2^q. \tag{D.8}$$

Further details on these correlations and their incorporation in the GNM is discussed in Raeini et al. (2017, 2018).

Appendix E. Direct flow simulations on pore space and fluid images

E.1. Single-phase flow properties

This section presents the results of direct single-phase flow simulations (DNS) using the OpenFOAM finite-volume library. We use the same formulation as in Raeini et al. (2012) but for single-phase flow only. The finite-volume mesh is generated directly from the micro-CT image of the pore space without smoothing the voxelization artefacts on the solid boundaries. The rationale behind using DNS instead of GNM is that GNM can predict DNS simulation results exactly if its flow conductivities are obtained from upscaling of the DNS results and can reproduce them closely when the conductivities are obtained using
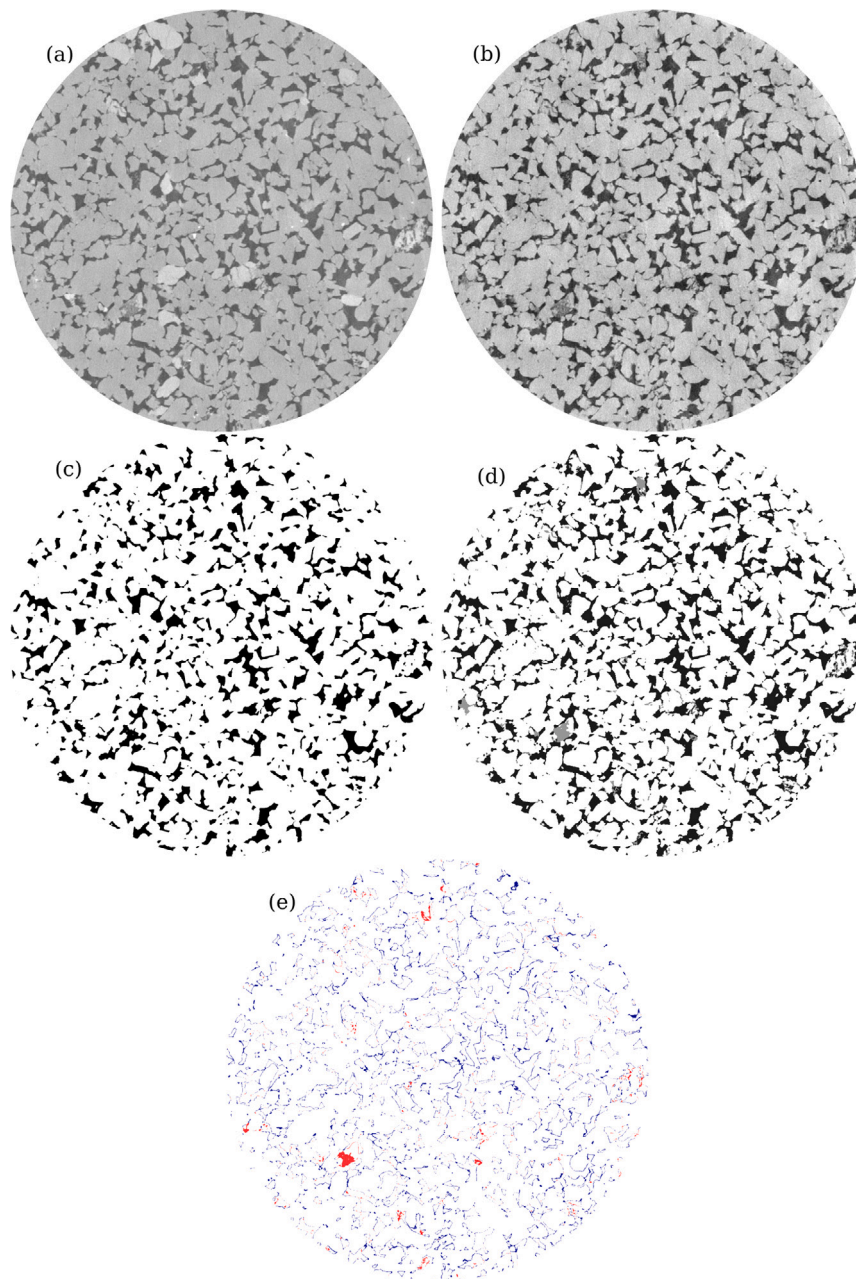
Fig. C.8. Slices at the middle of (a) dry and (b) differential (dry-water) images, (c) segmented dry image (Gao et al., 2020) and (d) the differential image segmented using the clustering algorithm presented in Appendix C, which shows the regions identified as sub-resolution or clay porosity in grey and the macro-pores in black. The discrepancy between the pore space for the two segmentations is highlighted in (e).

correlations (Raeini et al., 2017). Furthermore, the focus of this section is to study imaging and image processing artefacts while excluding any approximations which might be introduced during the network modelling workflow.

We have presented sensitivity studies for the effect of voxel size in Table E.2, for the effect of segmentation algorithm in E.3 and for the effect of surface morphology at the scale of the voxel sizes (3.58 μm) in Table E.4.

The results in Table E.2 show that voxel size plays an important role in the prediction of single-phase flow properties from micro-CT images, despite its minor role in the two-phase flow results presented in Section 5.2. The sensitivity of the single-phase flow properties to different segmentations of the void space in Table E.3 is also significant. Finally, surface morphology plays an important role both in prediction

Table E.2

Effect of voxel size on direct simulation of single-phase flow properties – porosity and absolute permeability, k_{abs}, and formation factor, FF, in the x, y and z Cartesian directions – of the high-resolution image with an original voxel size of $\delta x = 1.5\,\mu m$ provided by TotalEnergies.

Resample	δx (μm)	Porosity	k_x (D)	FF_x	k_y (D)	FF_y	k_z (D)	FF_z
1	1.5	0.188	1.713	19.00	1.826	18.34	1.764	19.17
2	3.0	0.169	1.193	25.70	1.364	24.82	1.246	25.98
3	4.5	0.151	0.767	36.98	0.915	34.97	0.805	36.99

of single-phase flow properties (Table E.4) as well as in the prediction of two-phase flow properties using the GNM formulation (see Fig. 5). Further investigation is needed to have a predictive workflow to obtain single-phase flow properties without input from experimental data.
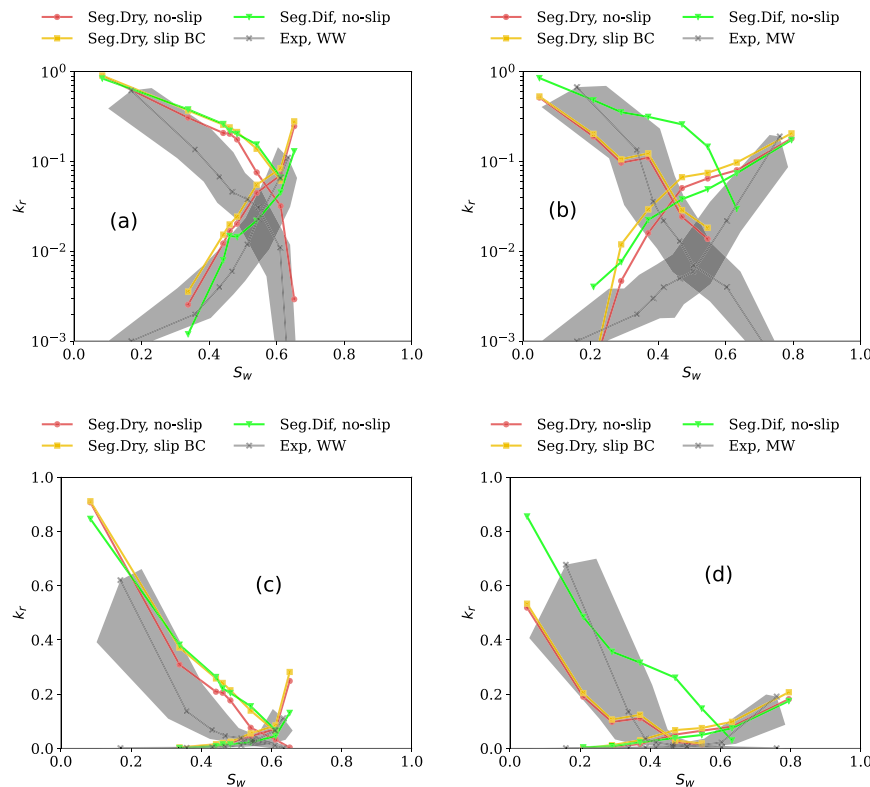
Fig. E.9. Relative permeabilities computed using direct numerical simulation (DNS) on segmented images of fluid phases taken during the experiments, which are plotted against the saturations based on the image segmentation and compared to the experimental data presented in Fig. 2. The top row shows the results on semi-log and the bottom plots are on a linear scale. The left column shows results for the water-wet (WW) case, while the right column shows the mixed-wet (MW) results. The fluid conductivities are computed by applying both slip and no-slip boundary conditions on fluid–fluid interfaces for the segmentation of fluid phases by Gao et al. (2020) ('Seg.Dry, no-slip' and 'Seg.Dry, slip BC' respectively). In the slip boundary condition, the gradient of velocity field is set to zero and no flow is permitted to cross the boundary. Additionally the DNS results are presented for the segmentation of fluid phases by clustering algorithm in Appendix C, using the no-slip boundary condition on the fluid–fluid interfaces ('Seg.Dif, no-slip'). The results show that image segmentation has a higher impact than the boundary condition applied on the fluid–fluid interfaces.

Table E.3

Measured and direct simulation of single-phase permeability. Note that the porosity values using segmentation are underestimated while the permeability values are overestimated, potentially due to missing sub-resolution surface features in the segmented images. The experimental results on the 10 cm^3 sample are provided by TotalEnergies.

Method	Size	ϕ	k_{abs} (D)	Explanation
Experimental	~10 cm^3	0.206	0.98	Helium porosity
Experimental	1.06 cm^3		0.956 ± 0.06	Gao et al. (2020)
Experimental	1.06 cm^3	0.203 ± 0.007		Differential imaging
DNS, seg.dry	49 mm^3	0.162	1.64	Macropores only
DNS, seg.dif	49 mm^3	0.188 ± 0.004	2.29 ± 0.13	Macropores only

Table E.4

Effect of surface morphology modification iterations on the predicted single-phase flow properties using DNS for the segmentation of differential image (Seg.dif) using the clustering algorithm described in Appendix C and the segmentation of the dry image using thresholding (Gao et al., 2020). Surface morphology is introduced by flipping the voxels on either side of the void–solid boundary with a probability of 0.25 successively in multiple iterations (first column).

Roughness level	Seg.dif			Seg.dry		
	ϕ	k_{abs} (D)	FF	ϕ	k_{abs} (D)	FF
0	0.188	2.34	20.7	0.162	1.65	31.9
2	0.185	1.10	28.4	0.159	0.75	44.4
4	0.181	0.91	31.9	0.156	0.59	51.6

E.2. Direct flow simulations on micro-CT images of individual fluids

In order to have an assessment of imaging and image processing artefacts, we have performed direct single-phase flow simulations on voxels assigned to each fluid phase in the images (Hussain et al., 2014; Berg et al., 2016) and plotted the simulation results in Fig. E.9. We have performed the simulations using both slip and no-slip boundary conditions on the fluid–fluid interface for the segmentation of fluid phases by Gao et al. (2020). The slip boundary condition simulates a case where there is no viscous drag force on the fluid–fluid interface while a no-slip boundary condition represents a high resistive drag force; either of these scenarios can occur during two-phase flow depending on the fluid viscosity and relative velocity. Furthermore, in this Figure, we have presented simulations on an alternative segmentation of the pore-space and fluid phases using the clustering algorithm presented in Appendix C, to have an assessment of the effect of image segmentation on the predicted flow conductivities.

The simulation results in Fig. E.9 using the slip and no-slip boundary conditions are similar (a difference of 13% on average). However, the results in this figure for the two segmentations of the fluid phases show that segmentation can have a major effect on the quantification of the flow conductivities and that higher resolution images are required to accurately quantify conductivities of the imaged fluid phases using direct single-phase flow simulations.

Regardless of the segmentation and boundary conditions chosen, the predictions of relative permeability are poor with a tendency to over-predict the flow conductance. This suggests that simply applying DNS on pore-space images, unless run on very high-resolution images, is not necessarily a reliable method to assess flow properties. The reason for this is that DNS cannot accurately capture flow in thin wetting layers in pore space corners, nor can it account for the effect of sub-resolution roughness. While pore network models simplify the pore-space geometry, they can empirically account for these effects to provide robust predictions.

Appendix F. Supplementary data

Supplementary material related to this article can be found online at https://doi.org/10.1016/j.advwatres.2022.104194. This includes plots of relative permeability and capillary pressure that were used to obtain the uncertainty ranges in the bar charts presented in the main manuscript, in SVG (scalable vector graphics) format. It additionally includes the raw data of the bar charts as CSV (comma separated value) ASCII text files and as SQLite database tables.

References

Akai, T., Alhammadi, A.M., Blunt, M.J., Bijeljic, B., 2019a. Modeling oil recovery in mixed-wet rocks: pore-scale comparison between experiment and simulation. Transp. Porous Media 127 (2), 393–414. http://dx.doi.org/10.1007/s11242-018-1198-8.

Akai, T., Lin, Q., Alhosani, A., Bijeljic, B., Blunt, M.J., 2019b. Quantification of uncertainty and best practice in computing interfacial curvature from complex pore space images. Materials 12 (13), http://dx.doi.org/10.3390/ma12132138.

Al-Khulaifi, Y., Lin, Q., Blunt, M.J., Bijeljic, B., 2019. Pore-scale dissolution by CO2 saturated brine in a multimineral carbonate at reservoir conditions: Impact of physical and chemical heterogeneity. Water Resour. Res. 55 (4), 3171–3193. http://dx.doi.org/10.1029/2018WR024137.

Alhammadi, A.M., AlRatrout, A., Singh, K., Bijeljic, B., Blunt, M.J., 2017. In situ characterization of mixed-wettability in a reservoir rock at subsurface conditions. Sci. Rep. 7, 10753. http://dx.doi.org/10.1038/s41598-017-10992-w.

Alpak, F.O., Riviere, B., Frank, F., 2016. A phase-field method for the direct simulation of two-phase flows in pore-scale media using a non-equilibrium wetting boundary condition. Comput. Geosci. 20, 881–908. http://dx.doi.org/10.1007/s10596-015-9551-2.

AlRatrout, A., Blunt, M.J., Bijeljic, B., 2018. Spatial correlation of contact angle and curvature in pore-space images. Water Resour. Res. 54 (9), 6133–6152. http://dx.doi.org/10.1029/2017WR022124.

AlRatrout, A., Raeini, A.Q., Bijeljic, B., Blunt, M.J., 2017. Automatic measurement of contact angle in pore-space images. Adv. Water Resour. 109, 158–169. http://dx.doi.org/10.1016/j.advwatres.2017.07.018.

Andrew, M., Bijeljic, B., Blunt, M.J., 2014a. Pore-scale contact angle measurements at reservoir conditions using X-ray microtomography. Adv. Water Resour. 68, 24–31. http://dx.doi.org/10.1016/j.advwatres.2014.02.014.

Andrew, M.G., Bijeljic, B., Blunt, M.J., 2014b. Pore-scale imaging of trapped supercritical carbon dioxide in sandstones and carbonates. Int. J. Greenhouse Gas Control 22, 1–14. http://dx.doi.org/10.1016/j.ijggc.2013.12.018.

Archie, G.E., 1942. The electrical resistivity log as an aid in determining some reservoir characteristics. Trans. AIME 146 (01), 54–62. http://dx.doi.org/10.2118/942054-G.

Armstrong, R.T., Porter, M.L., Wildenschild, D., 2012. Linking pore-scale interfacial curvature to column-scale capillary pressure. Adv. Water Resour. 46, 55–62. http://dx.doi.org/10.1016/j.advwatres.2012.05.009.

Berg, S., Rücker, M., Ott, H., Georgiadis, A., van der Linde, H., Enzmann, F., Kersten, M., Armstrong, R.T., de With, S., Becker, J., Wiegmann, A., 2016. Connected pathway relative permeability from pore-scale imaging of imbibition. Adv. Water Resour. 90, 24–35. http://dx.doi.org/10.1016/j.advwatres.2016.01.010.

Bijeljic, B., Mostaghimi, P., Blunt, M.J., 2011. Signature of non-fickian solute transport in complex heterogeneous porous media. Phys. Rev. Lett. 107, http://dx.doi.org/10.1103/PhysRevLett.107.204502.

Blunt, M.J., Lin, Q., Akai, T., Bijeljic, B., 2019. A thermodynamically consistent characterization of wettability in porous media using high-resolution imaging. J. Colloid Interface Sci. 552, 59–65. http://dx.doi.org/10.1016/j.jcis.2019.05.026.

Bultreys, T., Lin, Q., Gao, Y., Raeini, A.Q., AlRatrout, A., Bijeljic, B., Blunt, M.J., 2018. Validation of model predictions of pore-scale fluid distributions during two-phase flow. Phys. Rev. E 97, 053104. http://dx.doi.org/10.1103/PhysRevE.97.053104.

Bultreys, T., Singh, K., Raeini, A.Q., Ruspini, L.C., Øren, P.E., Berg, S., Rücker, M., Bijeljic, B., Blunt, M.J., 2020. Verifying pore network models of imbibition in rocks using time-resolved synchrotron imaging. Water Resour. Res. 56 (6), e2019WR026587. http://dx.doi.org/10.1029/2019WR026587.

Chapman, E.M., Yang, J., Crawshaw, J.P., Boek, E.S., 2013. Pore scale models for imbibition of CO2 analogue fluids in etched micro-model junctions using microfluidic experiments and direct flow calculations. Energy Procedia 37, 3680–3686. http://dx.doi.org/10.1016/j.egypro.2013.06.262.

DiCarlo, D.A., Sahni, A., Blunt, M.J., 2000. Three-phase relative permeability of water-wet, oil-wet and mixed-wet sandpacks. SPE J. 5 (1), 82–91. http://dx.doi.org/10.2118/60767-PA.

Fogden, A., Cheng, Q., Middleton, J., Kingston, A., Turner, M., Sheppard, A., Olson, T., Armstrong, R., 2015. Dynamic micro-ct imaging of diffusion in unconventionals. In: SPE/AAPG/SEG Unconventional Resources Technology Conference, San Antonio, Texas, 20-22 July 2015. pp. 1244–1259. http://dx.doi.org/10.15530/urtec-2015-2154822.

Foroughi, S., Bijeljic, B., Blunt, M.J., 2021. Pore-by-pore modelling, validation and prediction of waterflooding in oil-wet rocks using dynamic synchrotron data. Transp. Porous Media 138, 285–308. http://dx.doi.org/10.1007/s11242-021-01609-y.

Gago, P.A., Raeini, A.Q., King, P., 2021. A spatially resolved fluid-solid interaction model for dense granular packs/soft-sand. Adv. Water Resour. 136, 103454. http://dx.doi.org/10.1007/s11242-021-01609-y.

Gao, Y., Raeini, A.Q., Selem, A.M., Bondino, I., Blunt, M.J., Bijeljic, B., 2020. Pore-scale imaging with measurement of relative permeability and capillary pressure on the same reservoir sandstone sample under water-wet and mixed-wet conditions. Adv. Water Resour. 146, 103786. http://dx.doi.org/10.1016/j.advwatres.2020.103786.

Garfi, G., Cedric, M.J., Steffen, B., Samuel, K., 2020. The sensitivity of estimates of multiphase fluid and solid properties of porous rocks to image processing. Transp. Porous Media 131, 985–1005. http://dx.doi.org/10.1007/s11242-019-01374-z.

Glover, P.W.J., 2016. Archie's law – a reappraisal. Solid Earth 7 (4), 1157–1169. http://dx.doi.org/10.5194/se-7-1157-2016.

Gostick, J., Aghighi, M., Hinebaugh, J., Tranter, T., Hoeh, M.A., Day, H., Spellacy, B., Sharqawy, M.H., Bazylak, A., Burns, A., Lehnert, W., 2016. Openpnm: a pore network modeling package. Comput. Sci. Eng. 18 (4), 60–74. http://dx.doi.org/10.1109/MCSE.2016.49.

Hussain, W.V., and. Pinczewski, F., Cinar, Y., Arns, J.Y., Arns, C.H., Turner, M.L., 2014. Computation of relative permeability from imaged fluid distributions at the pore scale. J. Colloid Interface Sci. 104, 91–107. http://dx.doi.org/10.1007/s11242-014-0322-7.

Keller, A.A., Blunt, M.J., Roberts, P.V., 1997. Micromodel observation of the role of oil layers in three-phase flow. Transp. Porous Media 26 (3), 277–297. http://dx.doi.org/10.1023/A:1006589611884.

Moghadasi, L., Guadagnini, A., Inzoli, F., Bartosek, M., Renna, D., 2016. Characterization of two- and three-phase relative permeability of water-wet porous media through X-ray saturation measurements. J. Pet. Sci. Eng. 145, 453–463. http://dx.doi.org/10.1016/j.petrol.2016.05.031.

Morrow, N.R., 1970. Physics and thermodynamics of capillary action in porous media. Ind. Eng. Chem. 62 (6), 32–56. http://dx.doi.org/10.1021/ie50726a006.

Moss, A.K., Jing, X.D., Archer, J.S., 1999. Laboratory investigation of wettability and hysteresis effects on resistivity index and capillary pressure characteristics. J. Pet. Sci. Eng. 24 (2), 231–242. http://dx.doi.org/10.1016/S0920-4105(99)00045-5.

Mostaghimi, P., Blunt, M.J., Bijeljic, B., 2012. Computations of absolute permeability on micro-CT images. Math. Geosci. http://dx.doi.org/10.1007/s11004-012-9431-4.

Oak, M.J., 1988. A new X-ray absorption method for measurement of three-phase relative permeability. SPE Reserv. Eng. 3 (01), 199–206. http://dx.doi.org/10.2118/14420-PA, SPE–14420–PA.

Øren, P.E., Bakke, S., Arntzen, O.J., 1998. Extending predictive capabilities to network models. SPE J. 3 (04), 324–336. http://dx.doi.org/10.2118/52052-PA, SPE–52052–PA.

Pereira Nunes, J.P., Bijeljic, B., Blunt, M.J., 2016. Pore-space structure and average dissolution rates: a simulation study. Water Resour. Res. 52 (9), 7198–7212. http://dx.doi.org/10.1002/2016WR019313.

Raeini, A.Q., Bijeljic, B., Blunt, M.J., 2014. Direct simulations of two-phase flow on micro-CT images of porous media and upscaling of pore-scale forces. Adv. Water Resour. 231 (17), 5653–5668. http://dx.doi.org/10.1016/j.advwatres.2014.08.012.

Raeini, A.Q., Bijeljic, B., Blunt, M.J., 2017. Generalized network modeling: Network extraction as a coarse-scale discretization of the void space of porous media. Phys. Rev. E 96, 013312. http://dx.doi.org/10.1103/PhysRevE.96.013312.

Raeini, A.Q., Bijeljic, B., Blunt, M.J., 2018. Generalized network modeling of capillary-dominated two-phase flow. Phys. Rev. E 97 (1), 023308. http://dx.doi.org/10.1103/PhysRevE.97.023308.

Raeini, A.Q., Blunt, M.J., Bijeljic, B., 2012. Modelling two-phase flow in porous media at the pore scale using the volume-of-fluid method. J. Comput. Phys. 231 (17), 5653–5668. http://dx.doi.org/10.1016/j.jcp.2012.04.011.

Raeini, A.Q., Yang, J., Bondino, I., Bultreys, T., Blunt, M.J., Bijeljic, B., 2019. Validating the generalized pore network model using micro-ct images of two-phase flow. Transp. Porous Media 130 (2), 405–424. http://dx.doi.org/10.1007/s11242-019-01317-8.

Ramstad, T., Kristoffersen, A., Ebeltoft, E., 2020. Uncertainty span for relative permeability and capillary pressure by varying wettability and spatial flow directions utilizing pore scale modelling. E3S Web Conf. 146, 01002. http://dx.doi.org/10.1051/e3sconf/202014601002.

Regaieg, M., Bondino, I., Varloteaux, C., Faisal, T.F., Yang, J., Rivenq, R., 2021. Large two phase digital rock physics simulations for relative permeability uncertainty assessment. In: The 35th International Symposium of the Society of Core Analysts. pp. SCA2021–007.

Regaieg, M., Moncorgé, A., 2017. Adaptive dynamic/quasi-static pore network model for efficient multiphase flow simulation. Comput. Geosci. 21 (4), 1–12. http://dx.doi.org/10.1007/s10596-017-9661-0.

Reynolds, C.A., Krevor, S., 2015. Characterising flow behavior for gas injection: Relative permeability of CO2-brine and N2-water in heterogeneous rocks. Water Resour. Res. 51 (12), 9464–9489. http://dx.doi.org/10.1002/2015WR018046.

Rucker, M., Bartels, W.-B., Garfi, G., Shams, M., Bultreys, T., Boone, M., Pieterse, S., Maitland, G.C., Krevor, S., Cnudde, V., Mahani, H., Berg, S., Georgiadis, A., Luckham, P.F., 2020. Relationship between wetting and capillary pressure in a crude oil/brine/rock system: From nano-scale to core-scale. J. Colloid Interface Sci. 562, 159–169. http://dx.doi.org/10.1016/j.jcis.2019.11.086.

Sahimi, M., 2011. Flow and Transport in Porous Media and Fractured Rock: From Classical Methods to Modern Approaches. John Wiley & Sons, Hoboken, New Jersey.

Scanziani, A., Singh, K., Blunt, M.J., Guadagnini, A., 2017. Automatic method for estimation of in situ effective contact angle from X-ray micro tomography images of two-phase flow in porous media. J. Colloid Interface Sci. 496, 51–59. http://dx.doi.org/10.1016/j.jcis.2017.02.005.

Schlüter, S., Sheppard, A., Brown, K., Wildenschild, D., 2014. Image processing of multiphase images obtained via x-ray microtomography: A review. Water Resour. Res. 50 (4), 3615–3639. http://dx.doi.org/10.1002/2014WR015256.

Singh, K., Menke, H., Andrew, M., Lin, Q., Rau, C., Blunt, M.J., Bijeljic, B., 2017. Dynamics of snap-off and pore-filling events during two-phase fluid flow in permeable media. Sci. Rep. 7 (1), 5192. http://dx.doi.org/10.1038/s41598-017-05204-4.

Spurin, C., Bultreys, T., Bijeljic, B., Blunt, M.J., Krevor, S., 2019. Mechanisms controlling fluid breakup and reconnection during two-phase flow in porous media. Phys. Rev. E 100, 043115. http://dx.doi.org/10.1103/PhysRevE.100.043115.

Tartakovsky, A.M., Meakin, P., 2006. Pore scale modeling of immiscible and miscible fluid flows using smoothed particle hydrodynamics. Adv. Water Resour. 29 (10), 1464–1478. http://dx.doi.org/10.1016/j.advwatres.2005.11.014.

Valvatne, P.H., Blunt, M.J., 2004. Predictive pore-scale modeling of two-phase flow in mixed wet media. Water Resour. Res. 40 (7), W07406. http://dx.doi.org/10.1029/2003WR002627.

White, A.F., Brantley, S.L., 2003. The effect of time on the weathering of silicate minerals: why do weathering rates differ in the laboratory and field? Chem. Geol. 202 (3), 479–506. http://dx.doi.org/10.1016/j.chemgeo.2003.03.001.

Wildenschild, D., Sheppard, A.P., 2013. X-ray imaging and analysis techniques for quantifying pore-scale structure and processes in subsurface porous medium systems. Adv. Water Resour. 51, 217–246. http://dx.doi.org/10.1016/j.advwatres.2012.07.018.

Yang, J., Bondino, I., Regaieg, M., Moncorgé, A., 2017. Pore to pore validation of pore network modelling against micromodel experiment results. Comput. Geosci. 21 (5), 849–862. http://dx.doi.org/10.1007/s10596-017-9630-7.

Zahasky, C., Jackson, S.J., Lin, Q., Krevor, S., 2020. Pore network model predictions of Darcy-scale multiphase flow heterogeneity validated by experiments. Water Resour. Res. 56 (6), e2019WR026708. http://dx.doi.org/10.1029/2019WR026708.

Zhang, Y., Bijeljic, B., Gao, Y., Lin, Q., Blunt, M.J., 2021. Quantification of nonlinear multiphase flow in porous media. Geophys. Res. Lett. 48 (5), e2020GL090477. http://dx.doi.org/10.1029/2020GL090477.